

Modeling of surface-state induced inter-electrode isolation of n -on- p devices in mixed-field and γ -irradiation environments

N. Akchurin^a, T. Peltola^{a,*}

^aDepartment of Physics and Astronomy, Texas Tech University, 1200 Memorial Circle, Lubbock, Texas, U.S.A.

Abstract

Position sensitive n -on- p silicon sensors will be utilized in the tracker and in the High Granularity Calorimeter (HGCAL) of the Compact Muon Solenoid (CMS) experiment at High Luminosity Large Hadron Collider (HL-LHC). The detrimental effect of the radiation-induced accumulation of positive net oxide charge on position resolution in n -on- p sensors has typically been countered by the application of isolation implants like p -stop or p -spray between n^+ -electrodes. In addition to the positively charged layer inside the oxide and close to the Si/SiO₂-interface, surface damage introduced by ionizing radiation in SiO₂-passivated silicon particle detectors includes the accumulation of trapped-oxide-charge and interface traps. A previous study of either n/γ (mixed field)- or γ -irradiated Metal-Oxide-Semiconductor (MOS) capacitors showed evidence of substantially higher introduction rates of acceptor- and donor-type deep interface traps ($N_{it,acc/don}$) in mixed-field environment. In this work, an inter-pad and -strip resistance (or resistivity (ρ_{int})) simulation study of n -on- p sensors with and without p -stop isolation implants was conducted for both irradiation types. Higher levels of ρ_{int} showed correlation to higher densities of deep $N_{it,acc/don}$, with the inter-pad isolation performance of the mixed-field irradiated sensors becoming independent of the presence of p -stop implant between the n^+ -electrodes up to about 100 kGy. The low introduction rates of deep $N_{it,acc/don}$ in γ -irradiated sensors resulted in high sensitivity of ρ_{int} to the presence and peak doping of p -stop above the lowest dose of about 7 kGy in the study. As a consequence of the advantageous influence of radiation-induced accumulation of deep N_{it} on the inter-electrode isolation, position sensitive n -on- p sensors without isolation implants may be considered for future HEP-experiments where the radiation is largely due to hadrons.

*Corresponding author
 Email address: timo.peltola@ttu.edu (T. Peltola)

1. Introduction

In the position sensitive n -on- p particle detectors that will be utilized in the experiments of the High-Luminosity Large Hadron Collider (HL-LHC) like ATLAS and CMS, a parameter of particular concern is the preservation of position resolution in extreme radiation environments. This is due to the disadvantage of the n -on- p sensors where the segmented n^+ -electrodes can become shorted even when operated at high reverse bias voltages. The issue is caused by the radiation-induced accumulation of positive charge inside the passivation SiO_2 and close to the Si/SiO_2 -interface that can attract electrons to the interface in the inter-electrode gap to the extent that creates a conduction channel and compromises the inter-electrode isolation of the sensor. This is typically alleviated by placing an additional highly p -doped implant between the n^+ -electrodes that breaks the conduction channel, due to its negative space charge, by suppressing the electron density at the vicinity of Si/SiO_2 -interface. The two solutions commonly utilized to produce the isolation implants involve localized (p -stop) and uniformly distributed (p -spray) doping concentrations along the surface in the inter-electrode gap [1, 2, 3, 4, 5, 6, 7]. The p -spray approach adds one and p -stop two more lithography steps and additional ion implantations [8, 9] to the processing steps of a conventional p -on- n sensor, increasing the production cost of n -on- p sensors. Additionally, since high doping concentrations in the isolation implants have been observed to increase the probability of discharges or avalanche effects due to excessive localized electric fields [10, 7, 11], careful tuning of the processing parameters is required.

It should be noted that due to the positive oxide charge of SiO_2 at the Si/SiO_2 -interface (N_{ox}), the n^+ -electrodes without isolation implants are shorted by default already before irradiation, but as shown in [12], become isolated by the application of reverse bias voltage above the *threshold voltage of inter-electrode isolation* ($V_{\text{th,iso}}$) (e.g., $V_{\text{th,iso}} \leq 100$ V for $N_{\text{ox}} \leq 7 \times 10^{10} \text{ cm}^{-2}$).

Surface damage in SiO_2 -passivated devices induced by ionizing radiation (charged particles, X-rays or γ s) consists of the accumulation of a positively charged layer (fixed oxide charge density N_f that does not move or exchange charge with Si), trapped-oxide-charge and interface traps (or surface states N_{it}), along with mobile-ionic-charge (N_M) inside the oxide and close to the interface with silicon bulk. The mechanisms of surface-damage accumulation are described extensively in [13, 14, 15, 16, 17].

A previous study on inter-electrode resistance (R_{int}) performances of n -on- p sensors with p -stop or p -spray isolation implants irradiated either by protons or neutrons and γ s or the combination of the two up to estimated Total Ionizing Doses (TID) of about 1.5–2 MGy¹ showed high inter-strip isolation levels that,

¹Estimated by 1 kGy and 145 kGy per $1 \times 10^{14} \text{ n}_{\text{eq}} \text{ cm}^{-2}$ for neutrons [18] and protons [19], respectively, for the irradiation facilities

after the initial drop from the pre-irradiated level, remained essentially constant throughout the studied TID-range [10]. However, corresponding studies on X-ray irradiated n -on- p sensors with p -stop or p -spray [20] or solely p -stop [21] isolation implants displayed significant dose dependences, where R_{int} -values decreased by about two orders of magnitude between 0.5–100 kGy in [20] and 50–700 kGy in [21]. Additionally, when X-ray irradiations were complemented by n/γ -irradiations [21], the dose (or TID) dependence disappeared and high isolation levels were maintained for all TIDs in the study. Significantly, the higher-level inter-electrode isolation for irradiation types involving hadrons were found also for n -on- p sensors without isolation implants in [19]. In this study, the sensors irradiated by protons or n/γ s to estimated TIDs of 870 and 6 kGy, respectively, displayed substantially higher R_{int} -levels to a sensor X-ray irradiated to a dose of 3 kGy. These observations suggest that hadron or mixed-field irradiation induces higher rates of surface states with beneficial influence on inter-electrode isolation compared to X-ray irradiation.

This investigation focuses on the correlation between the introduction rates of deep acceptor- and donor-type interface traps ($N_{\text{it,acc/don}}$) and inter-electrode isolation in mixed-field or γ -irradiated n -on- p sensors with and without p -stop isolation implants. The study presented here is a continuation of the investigation reported in [22], where the parameters of the components of the radiation accumulated net $N_{\text{ox}} - N_{\text{f}}$ and deep $N_{\text{it,acc/don}}$ (no evidence of N_{M} was detected) – were extracted by reproducing by simulation the CV -characteristics of n/γ (i.e., a mixed field)- or γ -irradiated MOS-capacitors. Motivated by the observed significant differences in the introduction rates of $N_{\text{it,acc/don}}$, the investigation was extended to a comparison of the simulated R_{int} (or resistivity (ρ_{int})) performances between the two irradiation types. By applying the extracted N_{f} and $N_{\text{it,acc/don}}$ at the Si/SiO_2 -interface between n^+ -electrodes of n -on- p sensor structures, ρ_{int} -simulations were initiated for the mixed field in the previous study and completed for both irradiation types in this investigation. The results were produced by sensors structures with dimensions and parameters of CMS High Granularity Calorimeter (HGCAL) [23] pad sensors and test-strips.

The paper is arranged by first discussing in Section 2 the observations on oxide-charge and surface-state accumulation with dose (D), based on the results extracted in ref. [22]. Next, the simulation setup, modeled sensor structures and methods used to derive inter-electrode resistivity are described in Section 3. Inter-electrode isolation results in Section 4 start with simulated ρ_{int} performance of a pre-irradiated sensor with and without p -stop in Section 4.1. Corresponding results for mixed-field and γ -irradiated sensors are presented in Section 4.2, followed by the comparison between measured and simulated ρ_{int} performances of

in [10].

Table 1: The simulation input parameters of radiation-induced N_{it} from ref. [22]. $E_{a,V,C}$ are the activation energy, valence band and conduction band energies, respectively, while $\sigma_{e,h}$ are the electron and hole trapping cross sections, respectively.

N_{it} type	E_a [eV]	$\sigma_{e,h}$ [cm 2]	Density [cm $^{-2}$]
Deep donor ($N_{it,don}$)	$E_V + 0.65$	1×10^{-15}	see column 5 in Table 2
Deep acceptor ($N_{it,acc}$)	$E_C - 0.60$	1×10^{-15}	see column 6 in Table 2

X-ray and γ -irradiated sensors in Section 4.3. Finally, the results are discussed in Section 5, while summary and conclusions are given in Section 6.

2. Observations on oxide-charge and surface-state accumulation with dose

The experimental and simulation study presented in ref. [22] of MOS-capacitors n/ γ -irradiated at the Rhode Island Nuclear Science Center² (RINSC) and UC Davis McClellan Nuclear Research Center³ (MNRC) reactors or γ -irradiated at Sandia National Laboratories Gamma Irradiation Facility⁴ (GIF) led to the extracted surface-state parameters in Table 1 with densities presented in Table 2. This process was carried out by tuning the parameters in a Technology Computer-Aided Design (TCAD)-simulation until close agreement with measured CV -characteristics of the irradiated MOS-capacitors was reached.

The TIDs in Table 2 for MNRC were determined by Monte Carlo N-Particle Transport (MCNP) simulations, which are in line with the reported TID-rate of 1 kGy per 1×10^{14} n_{eq}/cm 2 at Jožef Stefan Institute reactor facility (JSI) [24, 18] – a site widely utilized in the Si-device R&D within CMS and ATLAS – that has a similar TRIGA Mark II-design to the MNRC reactor. Since reactor-specific TID-estimates were not available for RINSC and due to the similar open-pool-reactor types of all three facilities with comparable power between RINSC and MNRC (2.0 and 2.3 MW, respectively), the aforementioned TID-rate was considered as a reasonable estimate also for RINSC TIDs, shown in Table 2.

After irradiation, the net oxide charge density at the Si/SiO₂-interface can be described as [22]

$$Q_{ox} = eN_{ox} = e(N_f + aN_{it,don} - bN_{it,acc}), \quad (1)$$

where e is the elementary charge and a and b are the fractions of occupied $N_{it,don}$ and $N_{it,acc}$, respectively.

²<http://www.rinsc.ri.gov/>

³<https://mnrc.ucdavis.edu/>

⁴<https://www.sandia.gov/research/gamma-irradiation-facility-and-low-dose-rate-irradiation-facility/>

Table 2: Neutron fluences, TIDs, CV -sweeps initialized from inversion (Inv., minority carriers at the Si/SiO₂-interface) and accumulation (Acc., majority carriers at the interface) modes of MOS-capacitor operation. Also given are the TCAD-simulation input densities for fixed oxide charge (N_f) and donor- and acceptor-type interface traps ($N_{it,don}$ & $N_{it,acc}$, respectively) from Table 1 to reproduce measured CV -characteristics of irradiated MOS-capacitors in ref. [22]. *) MCNP-simulated TIDs, ^T) Estimated TID ≈ 1 kGy per 1×10^{14} n_{eq}/cm² [24, 18]. Fluence = 0 indicates the γ -irradiated samples.

Fluence [$\times 10^{15}$ n _{eq} /cm ²]	TID/Dose [kGy]	CV-sweep	TCAD N_f [$\times 10^{12}$ cm ⁻²]	TCAD $N_{it,don}$ [$\times 10^{12}$ cm ⁻²]	TCAD $N_{it,acc}$ [$\times 10^{12}$ cm ⁻²]
0.35 ± 0.04	3.5 ± 0.3^T	Inv./Acc.	0.68	1.11	1.08
0.61 ± 0.05	$7.1 \pm 0.6^*$	Inv./Acc.	0.77	1.65	1.59
2.35 ± 0.19	23.5 ± 1.9^T	Inv./Acc.	1.00	2.30	2.60
6.6 ± 0.7	64 ± 7^T	Inv./Acc.	1.75	3.25	4.70
9.3 ± 1.1	$90 \pm 11^*$	Inv./Acc.	2.20	4.15	4.35
0	7.0 ± 0.4	Inv.	0.79	1.92	1.10
		Acc.	0.79	1.65	1.10
0	23.0 ± 1.2	Inv.	1.20	1.70	1.15
		Acc.	1.20	2.11	1.00
0	90 ± 5	Inv.	2.20	1.05	1.50
		Acc.	2.00	0.50	1.00

As shown in ref. [22], since the values of a and b change with applied gate voltage (V_{gate}) Q_{ox} in Eq. 1 can experience a polarity reversal with V_{gate} .

The differences in tuned values of N_f and $N_{it,don/acc}$ for γ -irradiated MOS-capacitors between CV -sweeps initialized either from accumulation- or inversion-regions are evident in Table 2. This is due to observed hysteresis in the respective CV -curves, which was found to be caused by the differences in the fractions of occupied $N_{it,don/acc}$ depending on the polarity of the initializing V_{gate} [22] (e.g., for CV -sweep starting from negative V_{gate} a larger fraction of $N_{it,don}$ will be occupied, resulting in a higher value of N_{ox} in Eq. 1). No hysteresis was observed in the CV -characteristics of mixed-field irradiated MOS-capacitors, resulting in a single set of N_f and $N_{it,don/acc}$ for a given TID in Table 2. Summary of MOS-capacitor modes of operation is given in Appendix A.

When the densities of the three components of N_{ox} from Table 2 are plotted as a function of dose in Figure 1, it is evident that while N_f -evolution is essentially equal for both of the irradiation types, N_{it} introduction

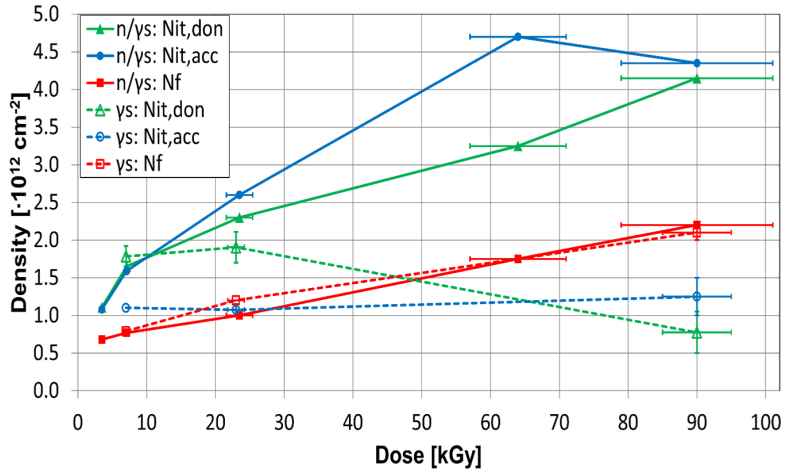


Figure 1: Simulated evolution of N_f and surface-state densities ($N_{it,acc/don}$) with dose at room temperature and frequencies between 1 – 9 kHz from Table 2 for mixed-field ('n/γs') and γ -irradiations. For clarity, mean values between densities extracted from CV -sweeps initialized either from accumulation- or inversion-regions of the γ -irradiated MOS-capacitors are considered.

rate for both donors and acceptors is substantially higher for the mixed-field environment. This difference in introduction rates of N_{it} could explain the previously reported better inter-strip isolation performance for mixed-field and hadron-irradiated n -on- p strip-sensors with or without isolation implants compared to the X-ray irradiated ones [19], due to the beneficial impact of radiation-induced accumulation of deep interface traps on the inter-electrode resistance (R_{int}) [22]. As discussed in ref. [22], the frequency- and temperature (f, T) dependence in the CV -characterizations introduced by the accumulation of N_{it} [13] could add a level of arbitrariness to the values of simulation extracted N_f and $N_{it,acc/don}$. Comparison with N_f and $N_{it,acc}$ extracted from capacitance/conductance-voltage and thermal dielectric relaxation current measurements of X-ray irradiated MOS-capacitors –considering the results for 700- and 750-nm-thick SiO_2 and $\langle 100 \rangle$ crystal orientation Si-bulk in Figures 9.6 and 9.7 in ref. [17]– shows similar densities and dose dependencies with the γ -irradiation results in Table 2 and Figure 1. Further comparison with measured N_{ox} and N_{it} results reported in [20] for MOS-capacitors (with 650-nm-thick SiO_2 and $\langle 100 \rangle$ Si-bulk) X-ray irradiated up to 100 kGy shows again similar values with γ -irradiation accumulated N_f and $N_{it,acc}$ presented here.

3. Simulation setup and methods

The 2D device-simulations were carried out using the Synopsys Sentaurus⁵ finite-element TCAD software framework. The simulations apply Neumann boundary and oxide-semiconductor jump conditions (potential jump across the material interface due to dipole layers of immobile charges), as well as Dirichlet boundary conditions for carrier densities and AC potential at Ohmic contacts that are used to excite the system. For the R_{int} -simulations, device-structures displayed in Figure 2 were implemented. The device in Figure 2a features the surface design dimensions between the cells of an HGCAL multi-channel sensor, while the device in Figure 2c reproduces the surface design of HGCAL test-strips. For the sensor-structure in Figure 2a, designs both with and without p -stop isolation implant were included in the simulations. Results from Spreading Resistance Profiling (SRP) measurements of the sensors carried out within HGCAL-community [25] were used as an input for the doping profiles in Figure 2b, while the passivation oxide thickness (t_{ox}) input was provided by the data from CV -characterizations of MOS-capacitors from HGCAL-sensor wafers. The bulk properties leakage current (I_{leak}) and full depletion voltage (V_{fb}) were set to match the measurements by tuning the charge carrier lifetimes ($\tau_{\text{e,h}}$) and bulk doping (N_{B}), respectively, while the crystal orientation $\langle 100 \rangle$ of the HGCAL sensor substrates was repeated in the bulk of the modeled devices. The components of radiation-induced surface damage, N_{f} and N_{it} from Table 2, were implemented at the Si/SiO₂-interface with a uniform distribution along the interface, which is an approximation of the real distribution that includes nonuniformities [13].

The simulated R_{int} was realized by applying a reverse bias-voltage (V_{bias}) from the backplane contact of the sensor, while either a low voltage V_{int} or no voltage is applied from one of the n^+ -electrodes and the resulting currents are observed on the adjacent electrode. R_{int} is then determined as

$$R_{\text{int}} = \frac{V_{\text{int}} - 0 \text{ V}}{I_{\text{leak}}(V_{\text{int}}) - I_{\text{leak}}(0 \text{ V})}, \quad (2)$$

by extracting the bulk-generated current $I_{\text{leak}}(0 \text{ V})$ from the surface current. The method yields identical results to the approach where at a discrete value of V_{bias} , I_{leak} is measured at multiple V_{int} (typically voltages between $\pm 5 \text{ V}$ to ensure linearity of $I_{\text{leak}}(V_{\text{int}})$) and R_{int} is extracted from the slope of $I_{\text{leak}}(V_{\text{int}})$ -plot. However, this procedure was chosen due to being substantially faster and less demanding on computing capacity since R_{int} for the full V_{bias} -range is given directly by the simulation. For straightforward comparison with sensors of varied geometries, R_{int} is normalized to ρ_{int} by the cross-sectional area A and the length l (82 and 77 μm

⁵<http://www.synopsys.com>

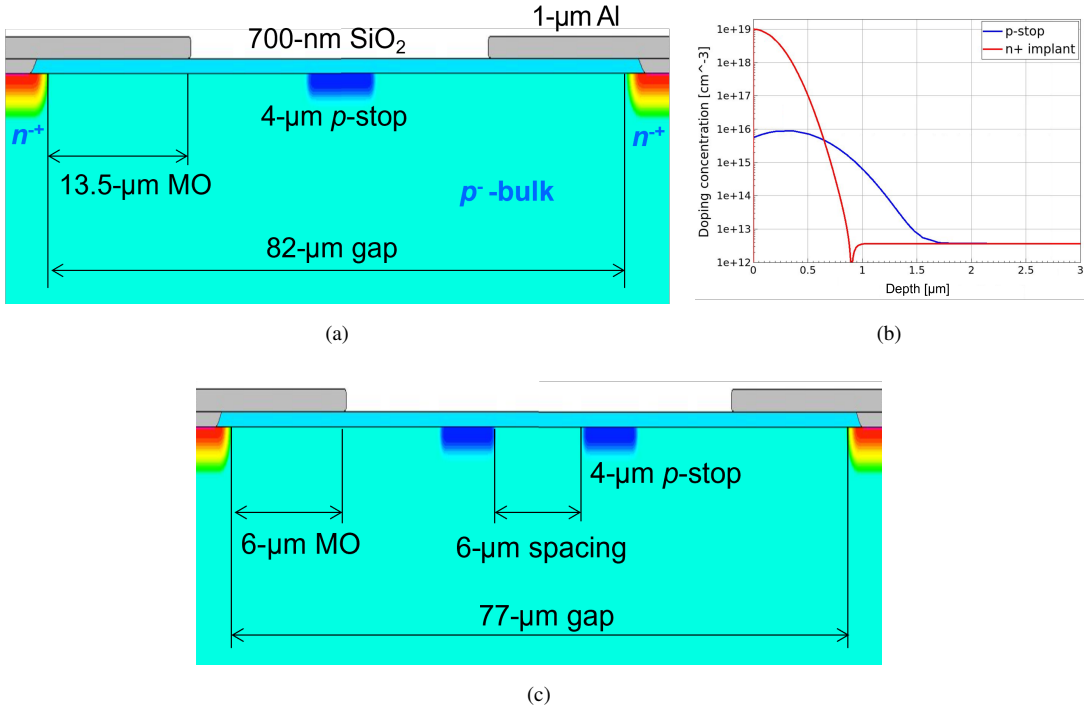


Figure 2: 2D-device structures implemented for the R_{int} -simulations. (a) Inter-pad region to 10-μm depth from the front surface of a DC-coupled 300-μm-thick n -on- p pad-sensor with a ‘common’ p -stop. MO = Metal-Overhang. A 700-nm-deep p^+ -blocking contact with 1-μm-thick uniform Al-layer was applied on the backplane of the sensor. (b) Doping profiles of the n^+ -implants and p -stop with $N_{\text{ps}} = 9.0 \times 10^{15} \text{ cm}^{-3}$. (c) Inter-strip region of a DC-coupled 300-μm-thick n -on- p strip-sensor with ‘individual’ p -stops. Features different from Figure 2a are indicated. Doping profiles are identical to Figure 2b, except for $N_{\text{ps}} = 1.5 \times 10^{16} \text{ cm}^{-3}$.

in Figures 2a and 2c, respectively) of the resistor as [26]

$$\rho_{\text{int}} = R_{\text{int}} \frac{A}{l} = R_{\text{int}} \frac{w \cdot d}{l}, \quad (3)$$

where w is the width of the electrode (i.e., length of the strip for strip-sensors) and d is the depth of the n^+ -implant (2 μm in Figure 2b).

4. Inter-electrode isolation results

The simulations in Sections 4.1–4.3 were carried out with the sensor-structure in Figure 2a, while Section 4.3 also applied the strip-sensor structure in Figure 2c.

4.1. Simulated: Pre-irradiated sensor

Figure 3 displays the ρ_{int} -results for a pre-irradiated reference sensor with and without p -stop isolation implant. As shown in ref. [22], before irradiation $N_{\text{ox}} \cong N_{\text{f}}$ which was set to $6.8 \times 10^{10} \text{ cm}^{-2}$ according to field-region N_{ox} results extracted from HGCAL sensors with oxide quality type ‘C’ in ref. [12].

The dashed black and orange lines in Figure 3 indicate the conservative estimates for the lower limits of sufficient inter-strip resistivity ($\rho_{\text{int,min}}$) for the CMS Tracker and HGCAL sensors, respectively. The difference between the two limits is due to the different limiting resistances in the biasing ($R_{\text{bias}} \approx 2 \text{ M}\Omega$ [27]) and readout (preamplifier input impedance of a few hundred Ω s) circuits of the AC-coupled Tracker and DC-coupled HGCAL sensors, respectively. The values of $\rho_{\text{int,min}}$ are determined by requiring $R_{\text{int,min}}$ to be about two orders of magnitude above the limiting circuit resistances ($\rho_{\text{int,min}}$ for the Tracker strips with $l = 75 \mu\text{m}$ and $w = 1.55 \text{ cm}$ is the corresponding value to the limit $R_{\text{int,min}} \times \text{strip length} = 100 \text{ M}\Omega \cdot \text{cm}$ used in refs. [19, 28], while $\rho_{\text{int,min}}$ for the HGCAL is a current estimation applied for this study). Even though all simulations in this study were carried out for DC-coupled HGCAL sensors in Figure 2 (simulated ρ_{int} is identical for AC- and DC-coupled devices) both $\rho_{\text{int,min}}$ limits are included in the following results as useful benchmarks.

The threshold voltage of inter-electrode isolation ($V_{\text{th,iso}}$) [12] in Figure 3 indicates the point where the attraction from the positively biased n^+ -pad on the electron layer in the inter-electrode gap overcomes the attractive force from the positive oxide charge of SiO_2 in the gap, which breaks the conduction channel and isolates the electrodes when the electrons are swept from the inter-electrode gap to the n^+ -pad. At $V > V_{\text{th,iso}}$ ρ_{int} becomes essentially independent of the p -stop implant, with absolute values as expected for pre-irradiated sensors [27].

4.2. Simulated: Mixed-field and γ -irradiated sensors

The parameters for N_{f} and N_{it} from Tables 1 and 2 were used as an input for the ρ_{int} -simulations in Figure 4 for five mixed-field and three γ -irradiation TIDs at $T = 253 \text{ K}$, that was commonly used measurement temperature in previously reported R_{int} -studies of irradiated strip-sensors [19, 28].

Since ρ_{int} results are extracted from DC-currents in Eq. 2, f, T -dependence of AC-measured CV -characteristics of irradiated MOS-capacitors discussed in Section 2 is reduced to T -dependence. The decrease of capture and emission rates of N_{it} with temperature results in lower surface current levels and thus higher absolute values of ρ_{int} at voltages where pads or strips are isolated.

As described in [22], for the mixed-field irradiated sensors the change of the effective bulk doping (N_{eff}) with neutron fluence induced displacement damage was approximated by tuning N_{eff} to obtain similar

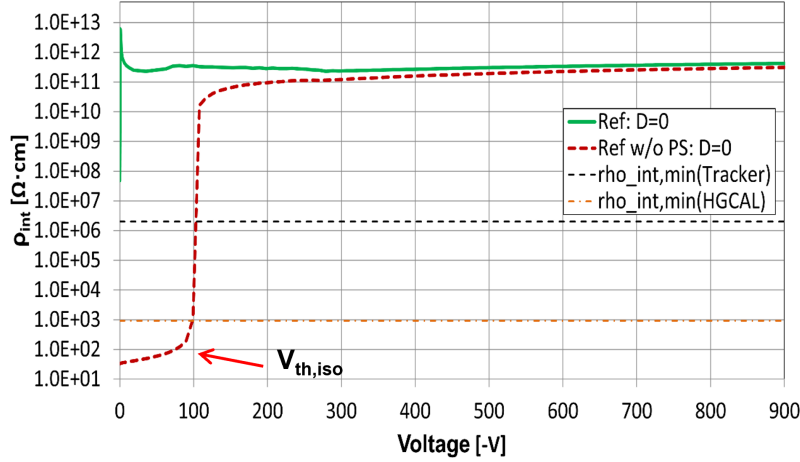


Figure 3: Simulated inter-electrode resistivity (ρ_{int}) for a pre-irradiated reference sensor at $T = 293$ K. Si/SiO₂-interface applied $N_{\text{ox}} \cong N_{\text{f}} = 6.8 \times 10^{10}$ cm⁻². Threshold voltage of inter-electrode isolation ($V_{\text{th,iso}}$) for the sensor without a *p*-stop implant ('w/o PS') is indicated, as well as estimates for the lower limits of sufficient inter-electrode isolation for the Tracker (2.0 M Ω · cm) and HGCAL (0.9 k Ω · cm) sensors.

minimum-capacitance to oxide-capacitance ($C_{\text{min}}/C_{\text{ox}}$) ratios with the MOS-capacitor measurements.

Presented in Figures 4a–4d, ρ_{int} for the mixed-field environment (green and violet curves) remains well above both $\rho_{\text{int,min}}$ levels at all voltages for the full TID-range from 3.5 ± 0.3 kGy to 90 ± 11 kGy. Also, it is evident that the *p*-stop implant is essentially irrelevant for the isolation of the n^+ -pads, which shows the beneficial impact of high introduction rate of N_{it} in Figure 1 on pad isolation. Corresponding results for γ -irradiated sensors in Figures 4a–4c (red and blue curves) display considerably lower ρ_{int} -levels above 7 kGy than for the mixed-field irradiated sensors with similar doses. The *p*-stop implant is now providing significant improvement on pad isolation at $D = 23.0 \pm 1.2$ kGy in Figure 4b (for *CV*-sweep starting from accumulation (Acc.), red curves), while at $D = 90 \pm 5$ kGy in Figure 4c limited benefit from *p*-stop starts taking place at $V > 800$ V, where ρ_{int} exceeds $\rho_{\text{int,min}}(\text{HGCAL})$ (for *CV*-sweep starting from inversion (Inv.), blue solid curve). The lower introduction rate of N_{it} with γ -irradiation compared to the mixed-field in Figure 1 correlates with the degrading pad-isolation performance with dose.

Figure 5 presents the evolution of ρ_{int} in Figures 3 and 4 with dose at 600 V (nominal operating voltage of HGCAL sensors for most of the expected fluence range [23]). For mixed-field irradiated sensors ρ_{int} remains essentially constant after the drop of about two orders of magnitude (at 3.5 ± 0.3 kGy) from the pre-irradiated level, and at least same amount above $\rho_{\text{int,min}}(\text{Tracker})$ for the full dose range, while again

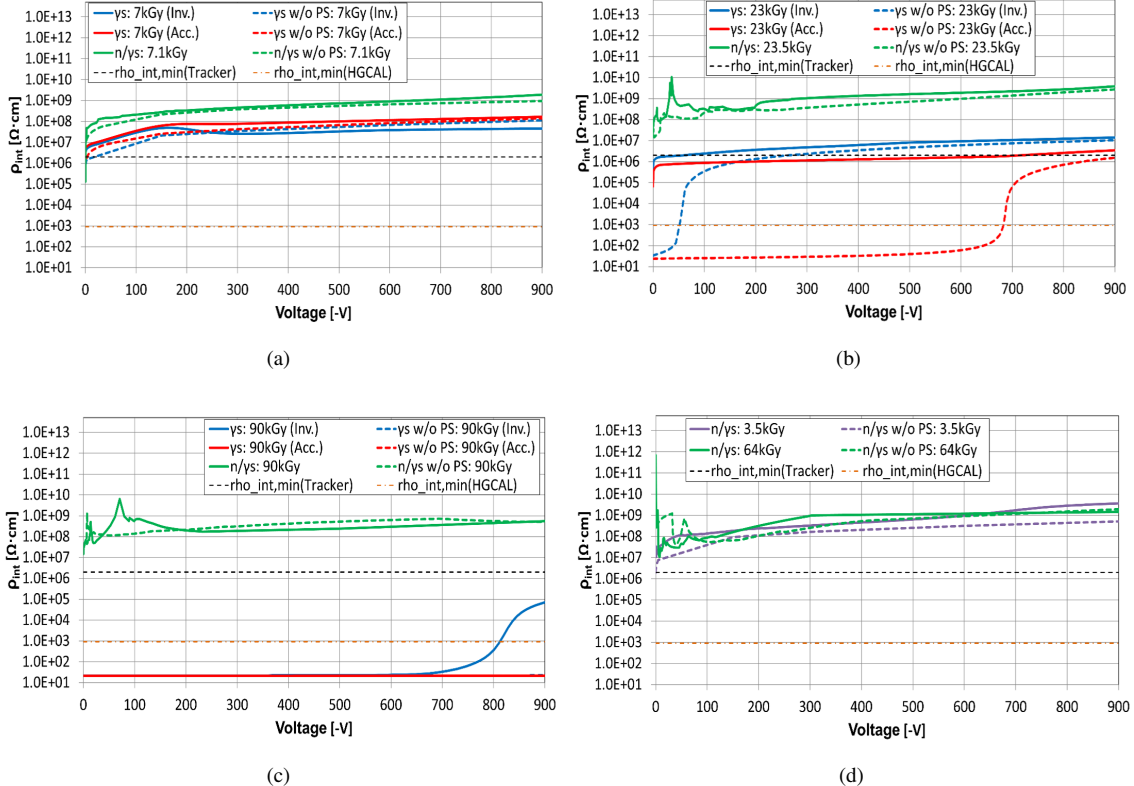


Figure 4: Simulated evolution of ρ_{int} with reverse bias voltage at $T = 253$ K for n -on- p sensors with and without p -stop implants γ - or mixed-field (n/γ) irradiated to (a) $D = 7.0 \pm 0.4$ kGy and TID = 7.1 ± 0.6 kGy, (b) $D = 23.0 \pm 1.2$ kGy and TID = 23.5 ± 1.9 kGy and (c) $D = 90 \pm 5$ kGy and TID = 90 ± 11 kGy, respectively. (d) Corresponding simulation results for the sensors mixed-field irradiated to TID = 3.5 ± 0.3 kGy and 64 ± 7 kGy, respectively. Surface-state and oxide charge parameters modeling the radiation-induced surface damage are given in Tables 1 and 2. Results obtained with parameters extracted from CV -sweeps started either from inversion ('Inv.') or accumulation ('Acc.') regions of the γ -irradiated MOS-capacitors are indicated in Figures 4a, 4b and 4c.

p -stop has a negligible role on the inter-pad isolation. At $D > 23$ kGy ρ_{int} for γ -irradiated sensors drops below $\rho_{\text{int,min}}(\text{Tracker})$ with significant benefit from p -stop on the pad isolation at 23 kGy (for CV -sweep starting from accumulation, red curves). At 90 ± 5 kGy the pads remain shorted with and without p -stops (red and blue curves). The distinctly different ρ_{int} performance at 23 kGy between parameter sets extracted from CV -sweeps starting either from inversion or accumulation for γ -irradiated sensors without p -stops

will be further discussed in Section 4.3. Thus, the correlation of the substantially different inter-electrode isolation performances between the two irradiation types to the different introduction rates of N_{it} is evident in Figures 4–5 and 1. Additionally, the general trends in the different ρ_{int} performances between γ - and n/γ -irradiated sensors are in line with the measured results between X-ray and X-ray + n/γ -irradiated sensors with p -stops in [21], where R_{int} of X-ray irradiated sensors keeps decreasing with dose, while remaining essentially constant for the mixed-field irradiated sensors.

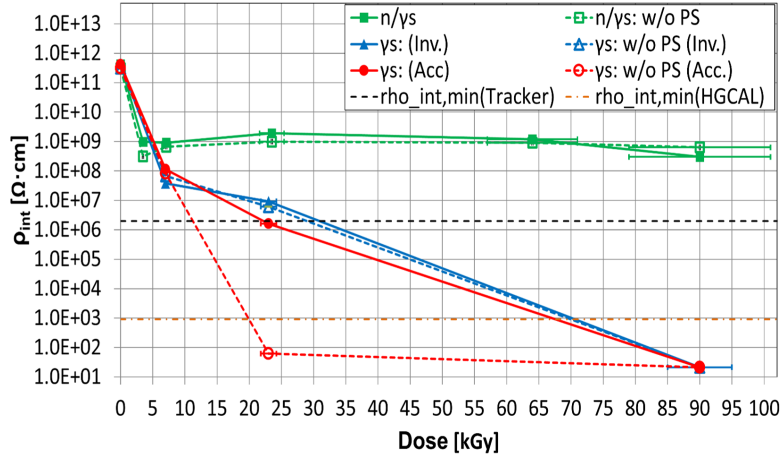


Figure 5: Simulated evolution of ρ_{int} with dose at $T = 253$ K and $V_{bias} = 600$ V, extracted from Figures 3 and 4.

Presented in Figure 6 is the comparison of the evolution of the Si/SiO₂-interface properties in the inter-electrode gap with the positive potential at the n^+ -pad between selected high and low ρ_{int} -performance sensors (two mixed-field and two γ -irradiated sensors) in Figure 4. Having the highest potential difference with respect to the n^+ -electrodes, the mid-gap in Figure 6 is the most revealing region on the interface, since it will be the first location where the conduction channel gets broken when the shorted electrodes become isolated by the bias voltage. Figure 6a shows the fraction of occupied $N_{it,don}$ (factor a in Eq. 1) from their total density in Table 2, that reflect closely the voltage dependence of the respective ρ_{int} in Figures 4a, 4b and 4c. For the γ -irradiated sensors, the correlation is prominent for the sensors without p -stop. This can be observed when the abrupt change from low to high values of ρ_{int} at about 100 and 700 V for sensors with 23.0 ± 1.2 kGy dose in Figure 4b (for N_f and N_{it} -parameters extracted for CV -sweeps from inversion or accumulation regions, respectively) is reflected as a change of factor a to non-zero values in Figure 6a (blue and red dashed curves). Similar but reversed-order correlation is apparent in the electron densities at the interface in Figure 6b, with

the electron density in the 23.0 ± 1.2 kGy γ -dose sensors dropping by about five orders of magnitude when high ρ_{int} -levels are reached in Figure 4b.

Correlation between N_{ox} -levels in Figure 6c and ρ_{int} can be observed in the two green curves for mixed-field irradiated sensors, where higher positive net N_{ox} -values result in lower ρ_{int} due to the increased attraction of electrons to the interface in the inter-electrode gap. While less pronounced, the same correlation applies also to the γ -irradiated sensors in Figure 6c (the values of N_{ox} at 900 V from the lowest to the highest ρ_{int} sensor are 2.46, 2.44 and $2.43 \times 10^{11} \text{ cm}^{-2}$, respectively). When the pads of the γ -irradiated sensor without p -stop are shorted at $V < 700$ V in Figure 4b the Si/SiO₂-interface in the inter-pad gap is filled by electrons, while hole access to the interface is restricted, leading to $a \rightarrow 0$ and $b \rightarrow 1$ in Eq. 1. As shown by the red curve for 23 kGy γ -irradiation in Figure 6c, net N_{ox} reaches then its minimum given by $N_{\text{ox}} = N_{\text{f}} - N_{\text{it,acc}}$, which remains constant until positive potential at the n^+ -pad becomes high enough to start removing electrons from the inter-pad gap. Hence, dynamic trends ($a > 0$ and $b < 1$) in the net N_{ox} -curves of the γ -irradiated sensors in Figure 6c indicate pad isolation. However, it is evident from Figure 6 that the different levels of ρ_{int} are reflected only by the evolution of occupied $N_{\text{it,don}}$ and electron density in Figures 6a and 6b, respectively.

4.3. Measured and simulated: X-ray and γ -irradiated sensors

As illustrated in Figures 4b, 4c and 5, ρ_{int} performances of γ -irradiated sensors show considerable sensitivity to the presence of p -stop implant with $N_{\text{ps}} = 9.0 \times 10^{15} \text{ cm}^{-3}$. Figure 7 shows ρ_{int} -results for the highest γ -irradiation dose of $D = 90 \pm 5$ kGy in Table 2 when N_{ps} is increased from its original level up to $3.0 \times 10^{16} \text{ cm}^{-3}$. It is evident that N_{ps} plays a critical role in inter-electrode isolation for γ -irradiated sensors. In addition, ρ_{int} performances display substantial differences depending on whether the parameters of N_{f} and N_{it} were tuned for *CV*-sweeps starting from either inversion ($\rho_{\text{int}}(\text{Inv.})$, solid curves) or accumulation ($\rho_{\text{int}}(\text{Acc.})$, dashed curves) regions. When N_{ps} is increased to $1.0 \times 10^{16} \text{ cm}^{-3}$ $\rho_{\text{int}}(\text{Inv.}) > \rho_{\text{int,min}}(\text{HGCAL})$ above 500 V, and for $N_{\text{ps}} = 1.5 \times 10^{16} \text{ cm}^{-3}$ $\rho_{\text{int}}(\text{Inv.})$ reaches $\rho_{\text{int,min}}(\text{Tracker})$ at about 700 V. On the other hand, $\rho_{\text{int}}(\text{Acc.})$ reaches high levels for voltages below 700 V only with $N_{\text{ps}} = 3.0 \times 10^{16} \text{ cm}^{-3}$, where ρ_{int} for both parameter sets is above $\rho_{\text{int,min}}(\text{Tracker})$ for all voltages.

To investigate which of the two aforementioned parameter sets of N_{f} and N_{it} tuned for $D = 90 \pm 5$ kGy models more accurately the real conditions at the Si/SiO₂-interface between n^+ -electrodes, the simulations were compared to the measured ρ_{int} of HGCAL test-strips in Figure 8. The test-strips were X-ray irradiated at CERN ObeliX facility [29] to $D = 100 \pm 10$ kGy (within uncertainty to the simulation model) and their dimensions and doping profiles were reproduced to the simulations as shown in Figures 2b and 2c. Since

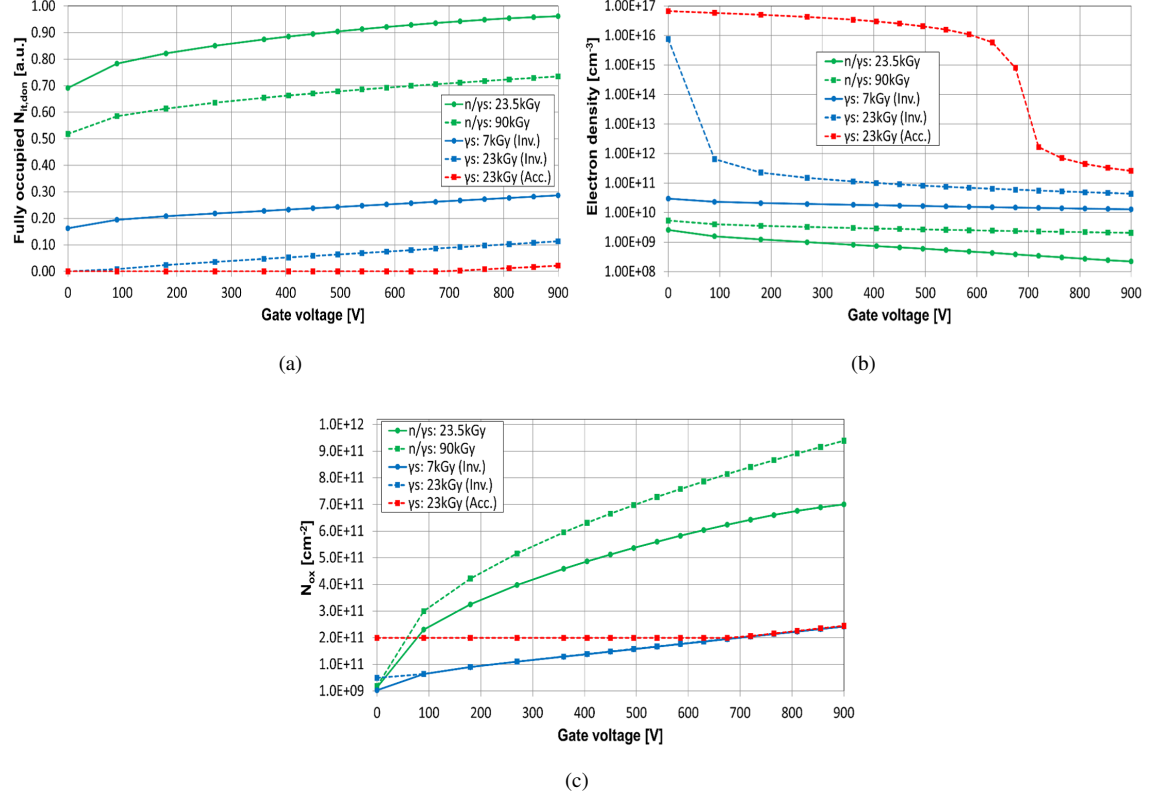


Figure 6: Simulated gate ($= n^+$ -electrode) voltage dependence of interface properties for high and low ρ_{int} cases, with cuts at Si/SiO₂-interface made at mid-gap between n^+ -implants in Figure 2a without p -stop. (a) Corresponding fractions of occupied $N_{\text{it,don}}$, (b) electron densities at the interface and (c) net N_{ox} to ρ_{int} -curves in Figures 4a (7.0 ± 0.4 kGy), 4b (23.0 ± 1.2 and 23.5 ± 1.9 kGy) and 4c (90 ± 5 kGy).

ρ_{int} performance is now strongly dependent on N_{ps} , its level in the test-strips was determined to be between $1.3 - 1.5 \times 10^{16} \text{ cm}^{-3}$ by MOSFET measurements carried out at HEPHY⁶ within the HGCAL collaboration. Displayed in Figure 8, when the upper value of the experimental N_{ps} is applied to the simulation, $\rho_{\text{int}}(\text{Inv.})$ (blue dashed curve) is in close agreement with the measurement throughout its voltage range, while $\rho_{\text{int}}(\text{Acc.})$ (red dash) remains in the levels where the strips are shorted for the most part of the investigated V_{bias} -range.

As a consequence, it is evident that the surface-damage parameter set extracted from the measurement

⁶Institut für Hochenergiephysik, Nikolsdorfer G. 18, Vienna, Austria.

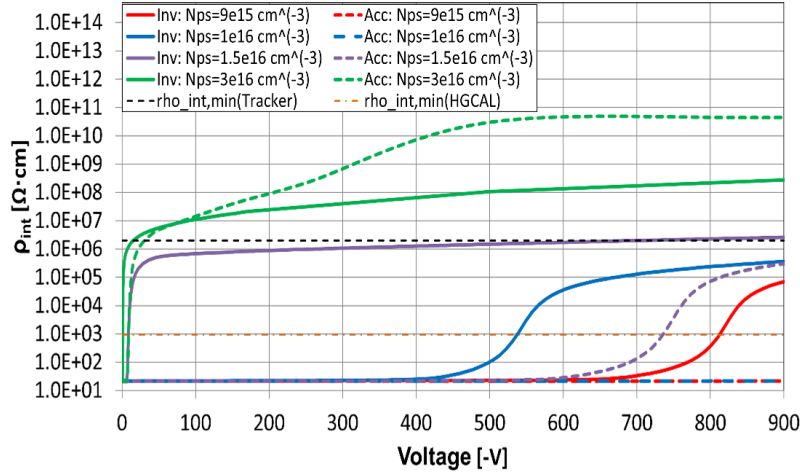


Figure 7: Simulated influence of N_{ps} on ρ_{int} at $T = 253$ K in a sensor γ -irradiated to $D = 90 \pm 5$ kGy. Results obtained with parameters extracted from CV -sweeps started either from inversion ('Inv.') or accumulation ('Acc.') regions of the γ -irradiated MOS-capacitors are indicated.

where the CV -sweep was started from negative voltages (inversion region in the case of the MOS-capacitor γ -irradiated to 90 ± 5 kGy in ref. [22] and Table 2), i.e., from the region where factor $a \rightarrow 1$ in Eq. 1, models more accurately the conditions at the Si/SiO₂-interface between reverse-biased n^+ -electrodes after X-ray or γ -irradiation. Also, higher introduction rates of N_f and $N_{it,acc/don}$ extracted from the inversion-region initialized CV -sweep in Table 2 are closer to the real circumstances in the inter-electrode gap.

5. Discussion

The correlation of the substantially different ρ_{int} performances between the mixed-field and γ -irradiated sensors in Section 4.2 to the different introduction rates of deep N_{it} in Section 2, suggests that X-ray or γ -irradiation testing of sensors targeted for mixed-field or hadron-dominated radiation environment can lead to overestimations on the degradation of the inter-electrode isolation with radiation. Additionally, since ρ_{int} was shown to be highly sensitive to the level of N_{ps} in Section 4.3, ρ_{int} -evaluations between passivation oxide variants by X-ray or γ -irradiations (e.g. possible differences in surface-state introduction rates at Si/SiO₂-interface) can be compromised by variations in N_{ps} between sensors, as influence from both the oxide quality and N_{ps} is convoluted. Therefore, careful assessment of the sample sensors is required to overcome the caveats associated with comparative studies on inter-electrode isolation by X-ray or γ -irradiations.

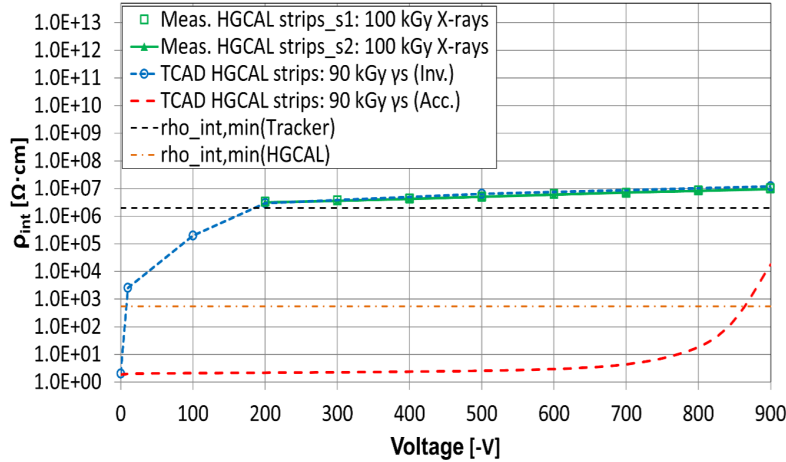


Figure 8: Comparison of measured and simulated ρ_{int} of irradiated HGCAL test-strips at $T = 253$ K. The two measured test-strip samples were X-ray irradiated to $D = 100 \pm 10$ kGy, while the simulation applied the surface-damage parameters for $D = 90 \pm 5$ kGy from Tables 1 and 2 and $N_{\text{ps}} = 1.5 \times 10^{16} \text{ cm}^{-3}$.

For mixed-field irradiated sensors, the simulated ρ_{int} displays high levels that remain essentially constant ($> 200 \text{ M}\Omega \cdot \text{cm}$ at 600 V in Figure 5) up to the highest dose of about 100 kGy in the study. The independence of the results on the presence of the p -stop isolation implant show the beneficial impact of the high introduction rates of deep N_{it} (due to the displacement damage caused by neutrons inside the oxide and at Si/SiO₂-interface [30]) on inter-electrode isolation. Thus, the results suggest that in mixed-field irradiated n -on- p sensors the inter-electrode isolation is predominantly provided by the radiation-induced accumulation of N_{it} rather than isolation implants or V_{bias} (as shown in Figure 3 and in ref. [12], V_{bias} in pre-irradiated sensor isolates n^+ -electrodes without p -stop).

The limiting factor of the reactor mixed-field irradiations in this study is the dose range. Where at the fluence of $1 \times 10^{16} \text{ n}_{\text{eq}} \text{ cm}^{-2}$ at HGCAL the expected ionizing doses are expected to be $1.0 - 1.5 \text{ MGy}$ [23], for similar fluence at the reactor radiation environment the ionizing dose is only about 100 kGy, as discussed in Section 2. However, when the reported saturation of the accumulation of N_{f} and N_{it} in SiO₂-passivated devices at X-ray doses of about 100–200 kGy [17, 20, 31] is considered also for mixed-field radiation, position resolution in n -on- p sensors without isolation implants could be expected to be maintained also in extreme radiation environments involving hadrons.

Since no gate voltage was applied during the MOS-capacitor irradiations in [22] that produced the surface

damage parameters in Tables 1 and 2, influence of electric field on the introduction rates of $N_{it,acc/don}$ was not investigated. The proton mechanism that generates interface traps, involves protons (hydrogen ions) created by ionizing radiation in the oxide drifting to the interface with silicon to produce dangling Si-bonds (i.e. interface traps) by breaking the hydrogenated Si-bonds at the interface. The main effect of a positive gate bias on proton mechanism is to remove the electrons thereby decreasing the fraction that recombine with the trapped holes. Conversely, a negative gate bias drives the protons away from the interface and consequently, they do not create interface traps. Decreased electron-hole recombination and increased proton reaction with the interface leads to higher N_{it} . Since n^+ -pads of HGCAL sensors will be positively biased during their operation, the electron separation from holes in the inter-pad gap by the electric field could result in increased introduction rates of N_{it} ⁷. The proton mechanism is described extensively in [32].

The influence of electric field distribution in the inter-pad gap of the 600-V biased HGCAL sensors on the spatial uniformity of mixed-field introduced N_{it} needs also to be considered. The approach of uniform N_{it} along the Si/SiO₂-interface applied in this study might then not accurately model the real spatial distribution when surface damage is introduced to the HGCAL sensors during their operation. As discussed in Section 4.2, the critical region for the inter-pad isolation is in the vicinity of the mid-gap. Within ± 10 μm from the mid-gap, for the two highest mixed-field (expected radiation type for HGCAL) fluences in the study the differences between minimum and maximum electric field values at 600 V were found to be about 4% (TID = 64 ± 7 kGy in Table 2) and 0.4% (TID = 90 ± 11 kGy) for sensors without p -stop. Thus, no significant variation of electric field in the region relevant to inter-pad isolation of HGCAL sensors was observed within the scope of this study.

Finally, the choice of device boundary at the Si/SiO₂-interface applied in this study was tested by changing the boundary to the outer surface of SiO₂ with an interface with 100- μm -thick layer of gas⁸, similar to the approach in [33]. While not identical, the inter-pad performance was observed to remain essentially the same throughout the voltage range for the new boundary, which will not affect the conclusions of this study. The comparison indicates that for a simulation study of inter-electrode isolation performance, the choice between the two boundaries is not critical.

⁷Electron removal from the inter-electrode gap to n^+ -pads by reverse bias voltage is shown in [12]

⁸ $N_f = 0$ and 10^{11} cm^{-2} at the SiO₂/gas-interface.

6. Summary and conclusions

The parameter-tuning of surface-damage components N_f and deep $N_{it,acc/don}$ to reproduce by TCAD simulation the CV -characteristics of MOS-capacitors irradiated either by γ s or a mixed field of neutrons and γ s showed significantly higher introduction rates of deep $N_{it,acc/don}$ for mixed-field irradiation [22]. When applied to inter-electrode resistance simulations of n -on- p pad-sensors up to doses of about 100 kGy, higher densities of deep $N_{it,acc/don}$ showed correlation with higher levels of ρ_{int} . The increase of ρ_{int} was found to be driven by the increase of the fraction of occupied $N_{it,don}$ and the decrease of electron density at the Si/SiO₂-interface in the inter-electrode gap, but not by the level of net N_{ox} . Additionally, comparison with measured ρ_{int} of X-ray irradiated strip-sensors indicated that the N_f and deep $N_{it,acc/don}$ extracted from CV -sweeps of γ -irradiated MOS-capacitors starting from negative voltages (i.e., higher fraction of occupied $N_{it,don}$) model more accurately ρ_{int} in X-ray or γ -irradiated n -on- p sensors.

Due to the lower introduction rates of deep $N_{it,acc/don}$ relative to mixed field, the simulated ρ_{int} of γ -irradiated sensors displayed high sensitivity to the presence and peak doping of a p -stop isolation implant above the lowest dose in the study. However, the presence of p -stop was irrelevant to the superior ρ_{int} performance of the mixed-field irradiated sensors throughout the investigated dose range. The results indicate that while the contribution from neutrons to TID is diminutive (MCNP-simulations for the MNRC reactor indicated 5% contribution to TID from neutrons [22]), their role in interface-trap introduction is decisive.

Thus, the beneficial impact of the high introduction rates of deep $N_{it,acc/don}$ on the inter-electrode isolation is evident in the results for the mixed-field radiation to the extent, where isolation implants between n^+ -electrodes are not required to maintain uncompromised position resolution in n -on- p sensors. Considering both the reported pre-irradiation isolation of n^+ -electrodes without isolation implant provided by sufficient V_{bias} (less than 200 V for typical values of N_{ox} in ref. [12]) and the apparent saturation of the accumulation of N_f and N_{it} at about 100 – 200 kGy, this configuration may be regarded as a possible n -on- p sensor candidate for future HEP-experiments with radiation environments involving hadrons. However, further experimental studies are required before n -on- p sensors without isolation implants can be considered a safe option. Finally, similar number of lithography and ion-implantation steps to p -on- n sensors would reduce the processing cost of n -on- p sensors, while the sensor performance of the isolation implantless configuration would benefit from the removal of the probability of discharges or avalanche effects due to excessive electric fields at the p -stops.

Acknowledgements

This work has been supported by the US Department of Energy, Office of Science (DE-SC0015592 and DE-SC0023690). We thank M. Defranchis and L. Diehl of CERN, and P. Á. Domínguez of ETH Zürich for providing the experimental data in the study.

Appendix A. MOS-capacitor modes of operation

The three modes of operation in the *CV*-characterizations of Metal-Oxide-Semiconductor (MOS) capacitors are accumulation, depletion and inversion. At gate voltages with $C/C_{\text{ox}} = 1$, where C and C_{ox} are the measured and oxide capacitances, respectively, the majority carriers (holes for *p*-bulk, electrons for *n*-bulk) are pulled to the Si/SiO₂-interface, forming an accumulation layer with zero surface potential. An abrupt drop of capacitance takes place in the depletion region, where the Si-surface is being depleted from majority carriers and measured C is now C_{ox} and depletion layer capacitance in series. Thus, the measured C keeps decreasing with gate voltage as the effective thickness of the depletion region, that acts as a dielectric between the gate and the Si-substrate, increases. Depth of the depletion region reaches its maximum, and measured C its minimum, when most of the available minority carriers are pulled to the Si/SiO₂-interface (by the positive oxide charge and by the negative gate voltage for *p*- and *n*-bulk MOS-capacitors, respectively), forming an inversion layer. The depletion region in the measured *CV*-curve is limited by the threshold voltage (V_{th}), where the surface potential equals twice the bulk potential, and the flat band voltage (V_{fb}), where the Si energy band becomes flat and the surface potential goes to zero [13, 22].

References

- [1] J. Kemmer, G. Lutz, Concepts for simplification of strip detector design and production, *Nucl. Instr. & Meth. A* 326 (1993) 209–213. doi:10.1016/0168-9002(93)90353-J.
- [2] R. H. Richter, et al., Strip detector design for ATLAS and HERA-B using two-dimensional device simulation, *Nucl. Instr. & Meth. A* 377 (1996) 412–421. doi:10.1016/0168-9002(96)00257-4.
- [3] Y. Iwata, et al., Optimal p-stop pattern for the N-side strip isolation of silicon microstrip detectors, *IEEE Trans. Nucl. Sci* 45 (3) (1998) 303–309. doi:10.1109/23.682398.

- [4] G. Verzellesi, G.-F. D. Betta, G. Pignateli, Compact modeling of n-side interstrip resistance in p-stop and p-spray isolated double-sided silicon microstrip detectors, in: 2000 IEEE Nuclear Science Symposium, IEEE, Lyon, France, 2000, pp. 25–27. doi:10.1109/NSSMIC.2000.949004.
- [5] C. Piemonte, Device simulations of isolation techniques for silicon microstrip detectors made on p-type substrates, *IEEE Trans. Nucl. Sci* NS-53 (3) (2006) 1694–1705. doi:10.1109/TNS.2006.872500.
- [6] Y. Unno, et al., Evaluation of test structures for the novel n⁺-in-p pixel and strip sensors for very high radiation environments, *Nucl. Instr. & Meth. A* 731 (2013) 183–188. doi:10.1016/j.nima.2013.04.075.
- [7] M. Printz, P-stop isolation study of irradiated n-in-p type silicon strip sensors for harsh radiation environments, *Nucl. Instr. & Meth. A* 831 (2016) 38–43. doi:10.1016/j.nima.2016.05.103.
- [8] J. Härkönen, et al., Low-temperature TCT characterization of heavily proton irradiated p-type magnetic Czochralski silicon detectors, *Nucl. Instr. & Meth. A* 583 (2007) 71–76. doi:10.1016/j.nima.2007.08.198.
- [9] G. Pellegrini, et al., Technology of p-type microstrip detectors with radiation hard p-spray, p-stop and moderated p-spray insulations, *Nucl. Instr. & Meth. A* 579 (2007) 599–603. doi:10.1016/j.nima.2007.05.253.
- [10] W. Adam, et al., P-Type Silicon Strip Sensors for the new CMS Tracker at HL-LHC, *JINST* 12 (2017) P06018. doi:10.1088/1748-0221/12/06/P06018.
- [11] R. Dalal, et al., Combined effect of bulk and surface damage on strip insulation properties of proton irradiated n⁺-p silicon strip sensors, *JINST* 9 (2014) P04007. doi:10.1088/1748-0221/9/04/P04007.
- [12] T. Abdilov, N. Akchurin, C. Carty, Y. Kazhykarim, V. Kuryatkov, T. Peltola, A. Wade, A method to observe field-region oxide charge and inter-electrode isolation from CV-characteristics of *n-on-p* devices, *JINST* 19 (2024) P09010, [arXiv:2402.04365]. doi:10.1088/1748-0221/19/09/P09010.
- [13] E. H. Nicollian, J. R. Brews, *MOS (Metal Oxide Semiconductor) Physics and Technology*, John Wiley & Sons, New York NY U.S.A., 1982.
- [14] T. P. Ma, P. V. Dressendorfer, *Ionizing Radiation Effects in MOS Devices and Circuits*, John Wiley & Sons, New York NY U.S.A., 1989.

- [15] T. R. Oldham, Ionizing Radiation Effects in MOS Oxides, World Scientific Publishing, Singapore, 1999.
- [16] J. R. Schwank, et al., Radiation Effects in MOS Oxides, *IEEE Trans. Nucl. Sci.* 55 (4) (2008) 1833–1853. doi:10.1109/TNS.2008.2001040.
- [17] J. Zhang, X-ray Radiation Damage Studies and Design of a Silicon Pixel Sensor for Science at the XFEL, Ph.D. thesis, University of Hamburg, DESY-2013-00115 (2013).
- [18] I. Mandić, et al., Bulk damage in DMILL npn bipolar transistors caused by thermal neutrons versus protons and fast neutrons, *IEEE Trans. Nucl. Sci.* 51 (4) (2004) 1752–1758. doi:10.1109/TNS.2004.832927.
- [19] J-O. Müller-Gosewisch and A. Dierlamm and A. Nürnberg, Influence of surface damage and bulk defects on the interstrip isolation of p-type silicon strip sensors, *JINST* 16 (2021) P07004. doi:10.1088/1748-0221/16/07/P07004.
- [20] F. Moscatelli, et al., Effects of Interface Donor Trap States on Isolation Properties of Detectors Operating at High-Luminosity LHC, *IEEE Trans. Nucl. Sci.* 64 (8) (2017) 2259–2267. doi:10.1109/TNS.2017.2709815.
- [21] V. Mariani, et al., Measurements of surface and bulk radiation damage effects in silicon detectors for Phase-2 CMS Outer Tracker, *Nucl. Instr. & Meth. A* 980 (2020) 164423. doi:10.1016/j.nima.2020.164423.
- [22] N. Akchurin, et al., Modeling of surface damage at the Si/SiO₂-interface of irradiated MOS-capacitors, *JINST* 18 (2023) P08001. doi:10.1088/1748-0221/18/08/P08001.
- [23] CMS Collaboration, The Phase-2 Upgrade of the CMS Endcap Calorimeter, CMS-TDR-019 (Nov. 2017).
- [24] M. Ravnik, R. Jeraj, Research reactor benchmarks, *Nuclear Science and Engineering* 145 (1) (2003) 145–152. doi:10.13182/NSE03-A2370.
- [25] V. Hinger, Silicon Sensor Process Quality Control for the CMS Phase-2 Upgrade, Ph.D. thesis, Vienna University of Technology, CERN-THESIS-2021-045 (2021).
- [26] G. F. Knoll, Radiation Detection and Measurement, 3rd ed., 3rd Edition, John Wiley and Sons, New York, 2000.

[27] F. Hartmann, Evolution of Silicon Sensor Technology in Particle Physics, 2nd Edition, Springer, 2017.
doi:10.1007/978-3-319-64436-3.

[28] J.-O. Müller-Gosewisch, Investigation of Radiation Damage in Silicon Sensors for the Phase-2 Upgrade of the CMS Outer Tracker, Ph.D. thesis, KIT, Karlsruhe, ETP, ETP-KA/2021-14 (2021).

[29] P. Vaiano, et al., Characterization of lab-on-fiber-based dosimeters in ultra-high dose radiation fields, *Optics & Laser Technology* 161 (2023) 109177. doi:10.1016/j.optlastec.2023.109177.

[30] H. F. A. Amir, A. Chik, Neutron radiation effects on metal oxide semiconductor (MOS) devices, *Nucl. Instr. & Meth. B* 267 (2009) 3032–3036. doi:10.1016/j.nimb.2009.06.051.

[31] F. Moscatelli, et al., Surface damage characterization of FBK devices for High Luminosity LHC (HL-LHC) operations, *JINST* 12 (2017) P12010. doi:10.1088/1748-0221/12/12/P12010.

[32] H. P. Hjalmarson, R. L. Pease, C. E. Hembree, R. M. V. Ginhoven, P. A. Schultz, Dose-rate dependence of radiation-induced interface trap density in silicon bipolar transistors, *Nucl. Instr. & Meth. B* 250 (2006) 269–273. doi:10.1016/j.nimb.2006.04.122.

[33] T. Poehlsen, et al., Charge losses in segmented silicon sensors at the Si-SiO₂ interface, *Nucl. Instr. & Meth. A* 700 (2013) 22–39. doi:10.1016/j.nima.2012.10.063.